



Thermodynamic analysis of production parameters and microstructural evolution in shape memory Ni(50-x)Ti(50)Fe(x) (x = 5, 10) alloy synthesized by combustion synthesis

Berk Keskin¹ · Bora Derin²

Received: 9 November 2023 / Accepted: 12 January 2024
© The Author(s) 2024

Abstract

This study represents an initial effort to produce NiTiFe shape memory alloys via the self-propagating high-temperature synthesis (SHS) process. The synthesis successfully yielded Ni₄₅Ti₅₀Fe₅ and Ni₄₀Ti₅₀Fe₁₀ alloys from elemental Ni, Ti, and Fe powders at three distinct preheating temperatures (240, 330, 420 °C). To support empirical findings, thermodynamic analysis using Factsage Thermodynamic Software was employed to correlate reaction propagation behavior with chemical composition. The calculation showed that the addition of 5 at.% Fe to the B2 phase did not hinder reaction self-propagation. This conclusion was supported with the $\Delta H_f/C_p$ ratio and transient liquid ratio, computed using the sub-lattice model, which closely resembled that of NiTi. Whereas 10 at.% Fe that synthesized at preheating temperature of 240 °C exhibits struggle, thus an increase in triggering time causes an effect on crystallite size and a decrease in porosity. Empirical results confirmed these findings, albeit influenced by ignition times. An increase in the liquid ratio due to the adiabatic temperature rise can also result in a reduction of NiTi content when the Fe ratio is increased, consequently diminishing the driving force for the reaction. In the sample containing –5% Fe, the main phase is B2, and the R martensitic phase is also present. Ms is determined to be –38.7 °C. SEM analyses revealed the presence of Ti₂Ni and Ti₂Ni₃ phases in the upper and lower regions, while the distribution in the middle section is more homogeneous. No martensitic transformation was observed in 10% Fe. Additionally, nanocrystalline regions were detected within the samples by transmission electron microscopy, contributing to a nuanced understanding of their structural properties.

Keywords Shape memory alloys · NiTiFe · SHS · Factsage · Thermodynamic

1 Introduction

NiTi shape memory alloys have attracted attention due to their superelasticity, corrosion resistance and mechanical properties. They are frequently used in space, biomedical fields [1]. The incorporation of a third element allows for the manipulation of NiTi's properties. The added substitutional element can change the transformation temperatures of the direct austenite to martensite transformation and of the reverse transformation from martensite to austenite as

well as superelasticity of alloy. According to the studies, Fe, Mn, Cr, Co, Al, and V are substituted for Ni, decreased the Ms temperature, this tends to stabilize the austenitic phase [2]. NiTi alloy with 5 at.% Fe addition has been reported to be harder than NiTi and alloys containing 5 at.% Nb, V, Si, Mg due to the solid solution strengthening [3]. While the localized corrosion resistance is weaker than that of NiTi, it is better than NiTiCu alloys [4]. However, the order of resistance to pitting and crevice corrosion is as follows: NiTi ≤ NiTiFe ≈ AISI316L < ASTM F138 < Ti₆Al₄V, and NiTi < AISI316L < ASTM F138 ≪ Ti₆Al₄V [5].

NiTiFe finds applications in space and medical fields. For instance, it can be utilized as coupling in hydraulic tube systems interacting within a narrow range at low temperatures, or in vibration damping damper systems with pseudo-elastic behavior across a wide temperature range. In medical applications, it can function as a vasodilator in cardiovascular applications or, in the form of a screw undergoing phase

✉ Berk Keskin
bkeskin@medipol.edu.tr

¹ Construction Technology Department, Istanbul Medipol University, Istanbul, Turkey

² Metallurgical and Materials Engineering Department, Istanbul Technical University, Istanbul, Turkey

transformation, apply additional pressure for the healing of fractured bones [6]. Krishnan et al. developed a helical thermally conductive spring effective in the As-R transformation in a system containing $\text{Ni}_{47.07}\text{Ti}_{49.66}\text{Fe}_{3.27}$. This spring functions in a cryogenic environment, operating between 298 and 233 K. It is responsible for the opening and closing tasks of the thermal system, achieving a displacement of 4 mm [7].

NiTiFe alloys were usually produced by vacuum arc remelting (VAM), vacuum induction melting (VIM) or mechanical alloying methods in the literature [8–11], but there were a few studies on that synthesized by the self-propagating high temperature synthesis (SHS) method. For instance, Moore et al. synthesized NiTiFe alloys by heating furnace slowly. It is called a thermal explosion, and an ignition wire is not used [12]. The SHS method is remarkable in that due to saving synthesis time and energy consumption. The most important differences from other methods are (1) the amount of porosity can be controlled by the preheating temperature. (2) The main phase (B2) can be intensely synthesized, besides the minor second intermetallic phases; for instance, when compared to the mechanical alloying method [11]. It usually doesn't change M_s temperature while affecting the mechanical properties [13]. As a result, the heating rate and the preheating temperature determine the porosity and second phases as Ti_2Ni , TiNi_3 , and Ni_4Ti_3 of the final product [14–17].

Several studies have been conducted on NiTi through combustion synthesis to control porosity. In this context, the preheating temperature is a crucial parameter since the exothermic energy provided for the reaction is low, aiming at self-propagation [15, 16, 18, 19]. Similarly, porosity can be controlled by adjusting the preheating temperature to produce bone-like implants. A low preheating temperature increases porosity by leading to a low combustion temperature and a low transition liquid, allowing the production of stiff, bone-like porous biomaterials [20–22]. A similar observation could be made for NiTiFe. While the recommended lowest preheating temperature for NiTi is between 150 and 200 °C, it is uncertain for Fe-doped NiTi due to limited studies on the subject.

While NiTiFe has been produced through various methods in the literature as discussed above, the studies specifically focusing on combustion synthesis with Fe-doped products are limited. Thermodynamic analyses in these studies have primarily compared the exothermic reaction heat formed by Ti-Fe to Ni-Ti, providing fundamental insights into the propagation of the reaction [12]. The porosities of products formed at different preheating temperatures and ratios, as well as the conditions of production and microstructural evolution, remain uncertain. In the current study, these gaps have been addressed largely by supporting them with thermodynamic modeling. In the current study, the samples were produced at different

preheating temperatures (240, 330, 420 °C) with different atomic ratios (5 and 10 at.% Fe) by the SHS method. The transformation temperatures, the macrostructure, the microstructure, and the crystal structures were examined for selected samples.

2 Experimental procedure

NiTi-Fe SMA was synthesized by the SHS method in the specially designed reactor. The experiments were carried out in the argon atmosphere to eliminate oxygen. For this purpose, the atmosphere in the reactor was vacuumed to the pressure of 10^{-3} mbar 2 times, and then it was filled to room pressure by high-purity argon gases. In each experiment, the W ignition wire (20 windings with a diameter of 2.5 mm, total length of 28 cm) was placed parallel (8–10 mm) above the sample for combusting synthesis. The ignition power was constant at about 650–700 W per second.

During the experiments, two variacs were used to control the heating of the ignition wire and the preheating temperature of the furnace for sample heating. The thermocouple (K-type) was placed in the middle of the vertical surface of the sample, and the computer recorded the temperature profile. Besides recording the temperature profile, the combusting wave was also recorded by an HD camera (60 fps) for a better understanding of the propagation.

The powders were used in the experiments as follows: > 99.9% purity Alfa Aesar powders Ni (3–7 microns), Ti (< 106 microns, spherical), and Fe (< 10 microns, spherical). All samples were prepared and sealed under an argon atmosphere and mixed for 12 h with ZrO_2 balls that were used to prevent clumping. The mixtures of the powders (6.3 g) were pressed in a cylinder shape under 65–70 MPa. The dimensions of each sample were ~ 11.75 mm in diameter, and ~ 12 mm in height.

For the sake of narrative simplicity, samples were assigned notations that represented the different experimental parameters, such as "S420d5" for the sample alloyed with 5% Fe and pre-heated to 410–420 °C.

After the SHS reaction, the samples were polished with sandpaper from 350 grits up to 2 μm diamond suspensions with suitable pads by auto polishing machine and then longitudinally cut with SiC cutting discs. Bruker D8 Advance X-Ray Diffractometer and Panalitic XRD (Philips) were carried out at room temperature, -150 and 200 °C with Cu K α radiation. The phase transformation (DSC analysis) was investigated by DSC Seiko 220 C device. A heating rate of 10 °C/min was chosen for the samples. The microstructure was also investigated by Hitachi SU70 FE model Scanning Electron Microscope (with EDS module), and to better

understand the crystal structure, JEM ARM 200CF (Jeol LTD, Tokyo/Japan) was used for TEM analysis.

3 Results and discussion

3.1 Thermodynamical investigation

Yi and Moore were the first researcher who tries to calculate adiabatic temperature to understand the propagation behavior of the NiTiFe alloys [12]. They calculated the formation enthalpy of NiTi and FeTi at 25 °C assuming, as they were pure substances. The calculation can be described as:

$$\Delta H_{T_c}^f = \Delta H_{T_{ig}}^f + \int_{T_{ig}}^{T_c} C_p dT = 0 \tag{1}$$

where $\Delta H_{T_c}^f$ and $\Delta H_{T_{ig}}^f$ are the formation enthalpy of the combusting and ignition temperature respectively. $\Delta H_{T_c}^f$ must be zero to ensure adiabatic condition. C_p is the heat capacity at constant pressure of the product. T_{ig} and T_c are ignition and combusting temperature, respectively. There is also an empirical formula for the reaction is self-propagating as follows [23]:

$$\Delta H_{(298^\circ K)}^f / \Delta C_{p(298^\circ K)} > 2000 K \tag{2}$$

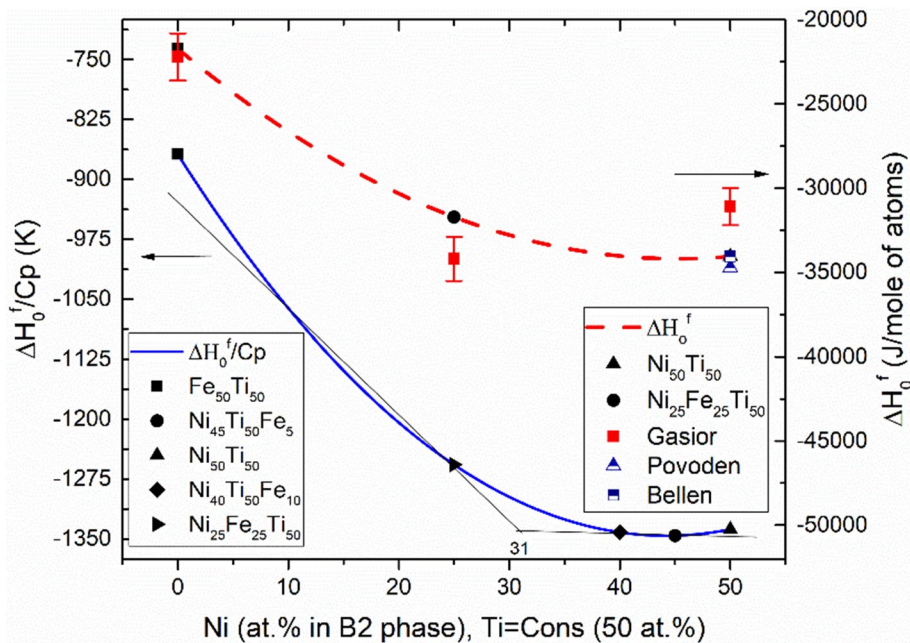
They related formation enthalpy of the products as follows:

$$Fe_{0.5}Ti_{0.5} < Ni_{(0.5-x)}Ti_{0.5}Fe_x < Ni_{0.5}Ti_{0.5}; x \leq 0.1 \tag{3}$$

There was no calculation of formation enthalpy on $Ni_{(1-x)}Ti_1Fe_x$. Their assumption was adding Fe to the NiTi for decreasing the combusting temperature, but in the real experiment, they indicated that adding Fe up to 10 at.% did not decrease the adiabatic temperature very much. As a result, the reaction easily propagated, and the product melted. The ignition temperature (~900 °C) was not changed for the NiTi and NiTiFe (< 10 at.% Fe) alloys. To understand this problem, the thermochemical calculations were carried out by the Factsage 8 Software with the SGTE 2017 Database. In the thermodynamic model, NiTi and NiTiFe were assumed as a solid solution, and the sub-lattice model was used utilizing the equilibrium mode of the software. With the help of this model, Fe was substituted into B2 ordered phase. As a result, the calculation provides more realistic results than the pure substance model.

In Fig. 1, ΔH_o^f (right y axis) and $\Delta H_o^f/C_p$ (left y axis) against Ni atomic ratio inside B2 phase is plotted. Ni and Fe vary in proportion to each other (50 at.%) while Fe atomic ratio (50 at.%) is fixed. As can be seen, value of $\Delta H_o^f/C_p$ of Ni₄₅Ti₅₀Fe₅ and Ni₄₀Ti₅₀Fe₁₀ are very close to each other (Ni₄₅Ti₅₀Fe₅ is slightly more negative value than Ni₄₀Ti₅₀Fe₁₀). It explains that there is no huge difference in propagation behavior between NiTi and Ni₄₅Ti₅₀Fe₅ experimentally. Additionally, two different slopes were encountered. The angle of the slope is high up to 31 at.% Ni, then it starts to stabilize and approaches 0 degrees. This also indicates that with the decreasing Ni content after 31 at.%, the reaction requires more energy, making its production through SHS more challenging because a decrease in nickel atomic content supports the formation of TiFe rather than NiTi. The enthalpy value for the formation of TiFe is more

Fig. 1 The value of $\Delta H_o^f/C_p$ respect to Ni at. ratio in NiTiFe. (Ni and Fe vary in proportion to each other (50 at.%), Ti (50 at.%) is constant)



positive, which means the reaction energy it generates for propagation will be lower.

To prove this calculation, the value is related with previous studies. The calorimetric studies on FeTi, NiTi, and TiNiFe were conducted by Gasior et al. and are comparable to Factsage calculations [24], but the enthalpy of NiTi phase was founded greater than studies of Bellen et al. and Povoden et al. [25, 26].

The pseudo phase diagram for NiTiFe and adiabatic temperature is shown in Fig. 2. In the diagram, the molar ratio of titanium is kept constant at 50 at.%, while the ratios of Ni and Fe change in a way that they add up to a total of 50 at.%. The liquid phase is not observed at 230 °C, and Ni₄₀Ti₁₅₀Fe₁₀'s adiabatic temperature is lower than Ni₄₅Ti₅₀Fe₅'s. Ni₄₅Ti₅₀Fe₅ reaches a greater adiabatic temperature at 320 °C than Ni₄₀Ti₅₀Fe₁₀. It also exhibits transient liquid formation (L/S(w)=0.353). It should be noted that a high liquid-to-solid ratio causes lower porosity[15].

However, at very high preheating temperatures (640 °C), it can lead to melting and the formation of voids in the middle of the sample [27]. In comparison to Ni₄₅Ti₅₀Fe₅, Ni₄₀Ti₅₀Fe₁₀ reaches a greater adiabatic temperature at 410 °C, but in contrast, it produces a less transient liquid phase, but it is enough to propagate reaction. When using a lower adiabatic temperature and a higher L/S ratio, the propagation becomes more challenging, whereas higher adiabatic temperatures and lower L/S ratios yield better propagation behavior but result in a highly porous structure. Additionally, the phase diagram in Fig. 2 illustrates that as the liquid ratio increases with adiabatic temperature, the proportion of Fe within it rises, especially for a high Fe (10 at.%) ratio. Consequently, as the energy contribution from the diminishing NiTi content in the transition liquid decreases, the driving force of the reaction also diminishes. In summary, increasing both the adiabatic temperature and the L/S (liquid-to-solid)

Fig. 2 Adiabatic temperature and liquid/solid mass ratio embedded on the pseudo phase diagram of Ni_(50-x)Ti₅₀-Fe_x

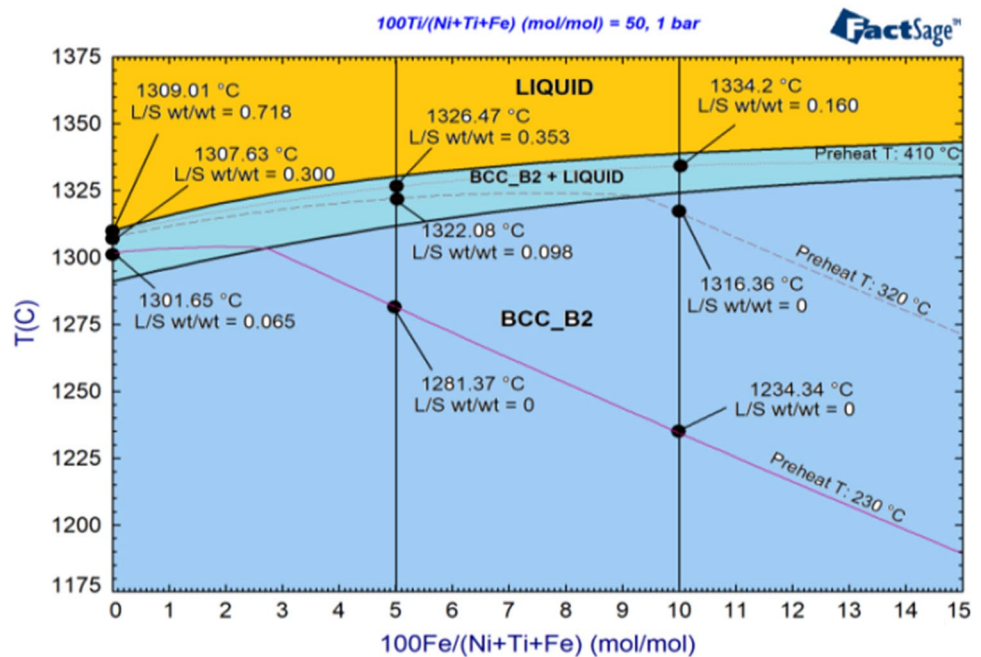


Table 1 Conditions and porosities for each reaction in SHS experiments

Preheating Temp	Ni ₄₅ Ti ₅₀ Fe ₅			Ni ₄₀ Ti ₅₀ Fe ₁₀		
	Preheating rate (°C/min.)	Ignition time/Propagation time (s.)	Outer and inner porosities	Preheating rate (°C/min.)	Ignition time/Propagation time (s.)	Outer and inner porosities
235–240 °C	25	6.32/3	29.34% 7.21%	23.3	29.5/2.6	25.7% 1.62%
320–330 °C	30.6	11.5/1	23.1% 0.6%	26.3	5.5/1 + 4*	17.5% 3%
410–420 °C	30.8	4/ < 1 + 2*	15% 2.1%	30.6	7/ < 1	10% 1%

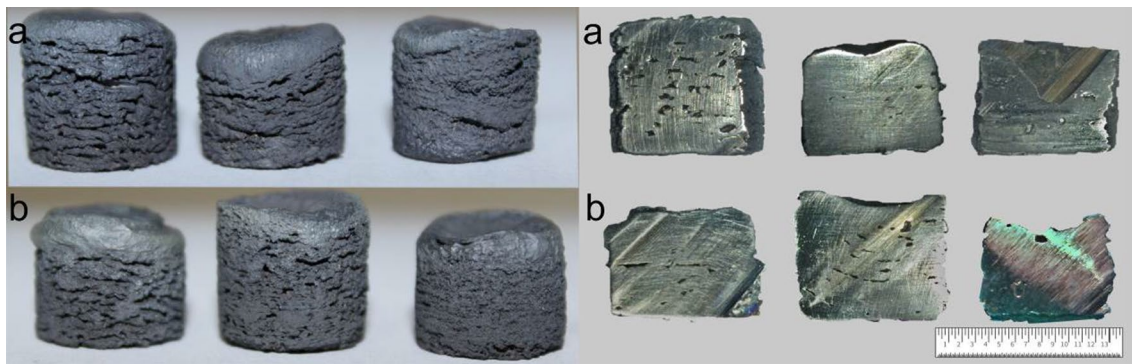


Fig. 3 Samples which is pre-heated to ~ 240 , ~ 330 , ~ 410 °C left to right for outer and cross-sectional surface **a** $Ni_{45}Ti_{50}Fe_5$, **b** $Ni_{40}Ti_{50}Fe_{10}$ (ruler in mm)

ratio in a reaction can result in the production of materials with reduced porosity and improved reaction propagation.

3.2 Relation between ignition time, pre-heating temperature and porosity

Table 1 presents data on the preheating rate, ignition, and propagation time, as well as porosities. Figure 3 offers visual representations, including cross-sectional and outer surface views. It's important to highlight that the total time specified in Table 1 may not correspond to the sum of propagation and ignition times. Any extra time beyond this sum is indicated by the "+ sec." notation, signifying that ignition persists even after propagation has concluded. For instance, in sample S330d10: After 5.5 s from ignition, the propagation started and completed in 1 s, but the triggering wire remained active for an additional 4 s.

Moore et al. demonstrated the rapid propagation at pre-heating temperatures of 900 °C [12]. The samples that were heated to 320–330 °C or higher in the current studies, propagated within a second of being ignited. Both samples were

made at 235–240 °C propagated in about 3 s, although it was discovered that the ignition of the S240d10 was challenging. Since there is no liquid generated at the adiabatic temperature (1234.3 °C), which can be determined from Fig. 2, S240d10 had trouble propagating in the current studies.

The reactions were triggered with W wire in the experiments, thus triggered time was also an important parameter for the sustainability of the synthesis. In other studies, a single-shot charged arc or laser-equipped system was typically utilized for the ignition instead of the ignition wire, but this method was not suited for alloyed NiTi(X) because the reaction was not typically self-sustained for the low pre-heating temperature (240 °C). Also, these methods are more expensive. To provide more heat energy for propagation, the triggered wire may be driven for a longer period. It also affects porosities and microstructure.

In Fig. 4, preheating temperature–time versus combusting temperature is depicted. The samples' lengths were reduced by raising the preheating temperature because it created a transient liquid phase as it moved through the voids, and it caused collapsing by reducing the porosity. As one of the

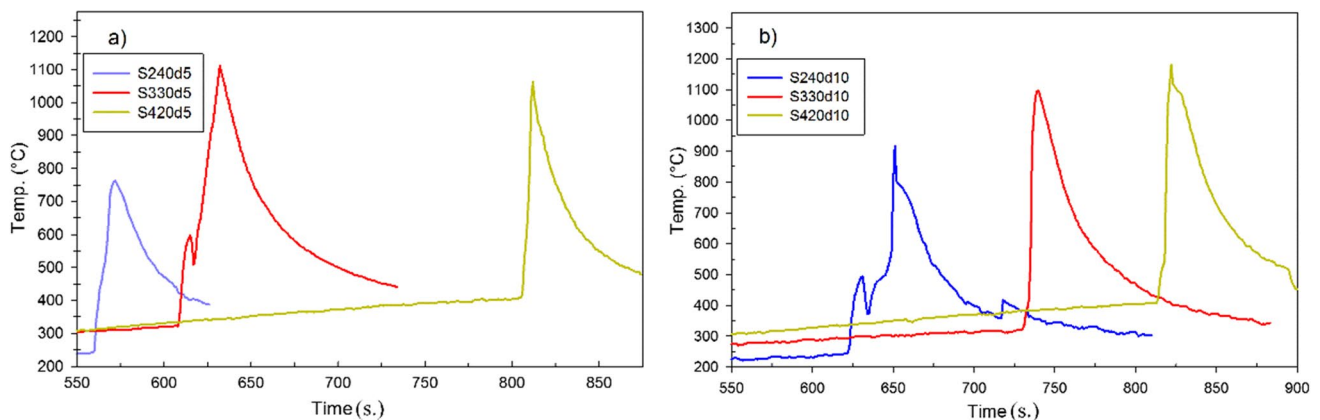


Fig. 4 Preheating regime versus time for all samples; **a** $NiTiFe_5$ **b** $NiTiFe_{10}$

drawbacks of synthesis with a trigger wire, it should be emphasized that since the wire is driven for a long period, the upper part is first affected. As a result, the upper sections of S330d5 and S240d10 melted because they reached higher temperatures before the propagation began. (Fig. 3).

When the cross-sectional surfaces were examined, there was no interconnection with the outer surface at the highest preheating temperature. Thus, most of this exhibited closed porosity. The ignition wire affects the adiabatic temperature as can be seen in Fig. 3. The outer porosity ratio of the $Ni_{45}Ti_{50}Fe_5$ was found to be slightly higher compared to the $Ni_{40}Ti_{50}Fe_{10}$, while the inner porosity exhibited a significant decrease. It can be explained as follows: (1) the ignited time of S240d10 was higher than S240d5 and it caused it to reach a higher combusting temperature (see Fig. 4). The luminosity of the S240d10 was also brighter than S240d5 (Fig. 5). This phenomenon can be attributed to the reduction in porosity coinciding with a potential increase in grain size. The elevated adiabatic temperature contributes to the formation of larger grains [28]. This is due to recrystallization and grain growth taking place after the completion of propagation, driven by the heat generated by the sample. [29]. It will be discussed in the next section. (2) S330d10 heated 4(*) seconds more after the ignition was completed, which possibly caused two successive combustion stages to make up the reaction process. This process affects the outer region of the sample, leading to a reduction in the outer porosity of S330d10. On the other hand, S330d5 achieved a higher combustion temperature due to its longer ignition time, resulting in the formation of parallel slits on the outer surface and a transient liquid-filled inner region. Consequently, the cross-sectional surface of S330d5 exhibited lower porosities (0.6%) compared to S330d10 (3%). (3) In S420d10, two successive combustion phases were also observed, and it reached a higher combusting temperature than S420d5 thus it reduced total porosity in both the inner and outer section and therefore has less porosity

than S420d5. A similar situation was observed in the study of Yeh et al. [15].

Lastly, comparing it to the calculated adiabatic temperature, the combustion temperature was found to be lower. It is probably caused by "the low pressing pressure (65 MPa)" and "the pre-heating rate (25–30 C/min.)" [17, 18, 30]. Various studies have reported that the rate of propagation of the reaction and the maximum adiabatic temperature increase with increasing preheating rate [15, 17]. Tosun et al., similarly, worked at 30 °C/min, 60 °C/min and 90 °C/min and stated that excessive liquid was formed and the compact shape deteriorated, especially after 60 °C/min. because the reaction reached higher exothermic energy [17, 30].

3.3 Microstructure investigation

According to the XRD results in Fig. 6, B2 phases are found in all samples besides Ti_2Ni and Ni_4Ti_3 (and/or Ti_2Ni_3) phases. No related B19' martensite peak is found in the samples. The unreacted Fe is also found in some samples.

A more detailed XRD was performed for S330d5 at different temperatures (25, -100, and 200 °C) to get more information about phase transformations. Figure 7 shows XRD spectra (speed of 1 degree/min.) with a 2-theta range of 10–100° at various temperatures. 200 °C is a sufficient temperature to transform retained martensite phase to the B2 phase, while –150 °C may not be the sufficient temperature to complete the transformation from R to B19'. As a result, the main peak of the R phase is indistinguishable due to very similar lattice parameters with B2 (around 42°), as well as other broadening sources (like stresses due to the presence of several secondary phases, thermal stresses, etc.) and lattice cell structure. Furthermore, a splitting peak at 78° corresponds to the (211) plane, which is attributed to a B2 to R transition. Mixtures of Ni_4Ti_3 and Ni_3Ti_2 phases are also found in 43.4°. It is very difficult to separate each other because both are metastable phases, and the peaks are very



Fig. 5 Propagation behavior of **a** S240d10 **b** S240d5 (0.166 s. for every frame. (0.166 s. for every frame. Total time = 3 s.)

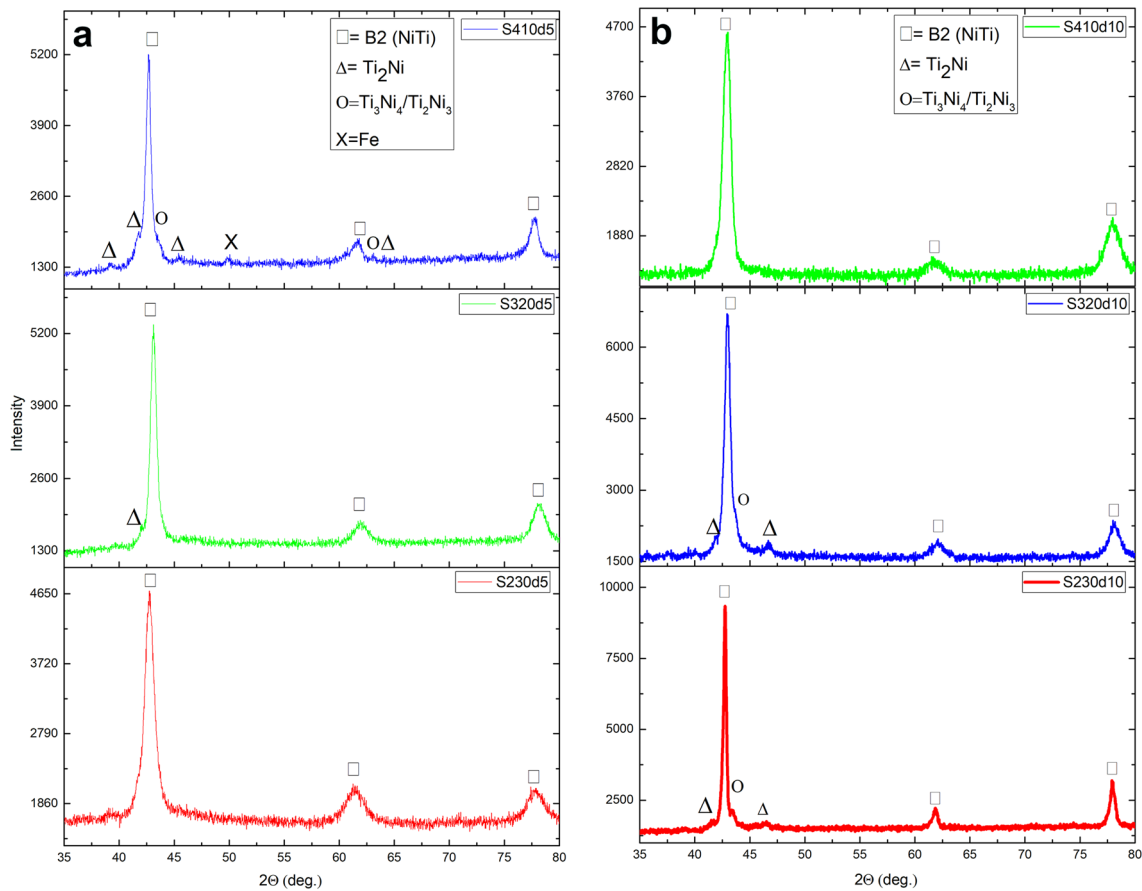


Fig. 6 XRD analysis for **a** *NiTiFe5*, **b** *NiTiFe10*

close to each other. In Raghavendra et al. study, longer aging time and higher temperatures lead to the transformation of Ni_4Ti_3 to $Ni_3Ti + Ni_3Ti_2$, which eventually results in Ni_3Ti [31]. Kaya et al. also found Ni_3Ti_2 and did not differentiate it from Ni_4Ti_3 in SHS. This was explained as a problem in the mixture of powder, even if the *Ni* and *Ti* atomic ratio is constant (50 at.%) [32].

Ni_4Ti_3 phase also supports R phase transformation because it suppresses the transformation of B2B19'. After all, a large nucleation barrier is needed for the transformation. As a result, the R phase easily nucleates on Ni_4Ti_3 due to better lattice matching. It needs further cooling to obtain B19' [33]. The study of Li indicated that increasing Fe in the casting, reduces the ratio of Ni_4Ti_3 , but this has not been observed in the present study [34].

X-ray profile analysis is a powerful method for estimating crystallite size. Williamson-Hall (W-H) analysis simplifies the integral breadth method by separating size-induced and strain-induced broadening based on peak width at 2θ [35].

With help of W-H, crystallite size is also calculated for selected sample. It can be simply expressed as:

$$\beta_{tot} \cos\theta = C\epsilon_{W-H} \sin\theta + \frac{K\lambda}{D_{W-H}} \quad (4)$$

where β_{tot} is total broadening (sum of broadening of crystallite size and strain), θ is Bragg angle, λ is wavelength of the X-ray source, K is constant (0.9), $C\epsilon_{W-H}$ is strain term, and D is crystallite size. When the $\beta_{tot} \cos\theta$ versus $\sin\theta$ is plotted, the crystallite size can be obtained from intercept of $K\lambda/D$, while the slope will be the strain. As discussed earlier, a longer ignition wire heating time results in higher combustion temperature and a larger crystallite size. S240d10 is heated for 29.5 s, while S240d5 is heated for 6.32 s. Consequently, crystallite sizes of 68, 27, 18, 140 nm are observed for S240d10, S330d10, S240d5 and S330d5 respectively. S330d5 achieves the highest combustion temperature among 5 at.% Fe with long triggering time (11 s.), but the value is larger than expected. It may be related to overlapping peaks

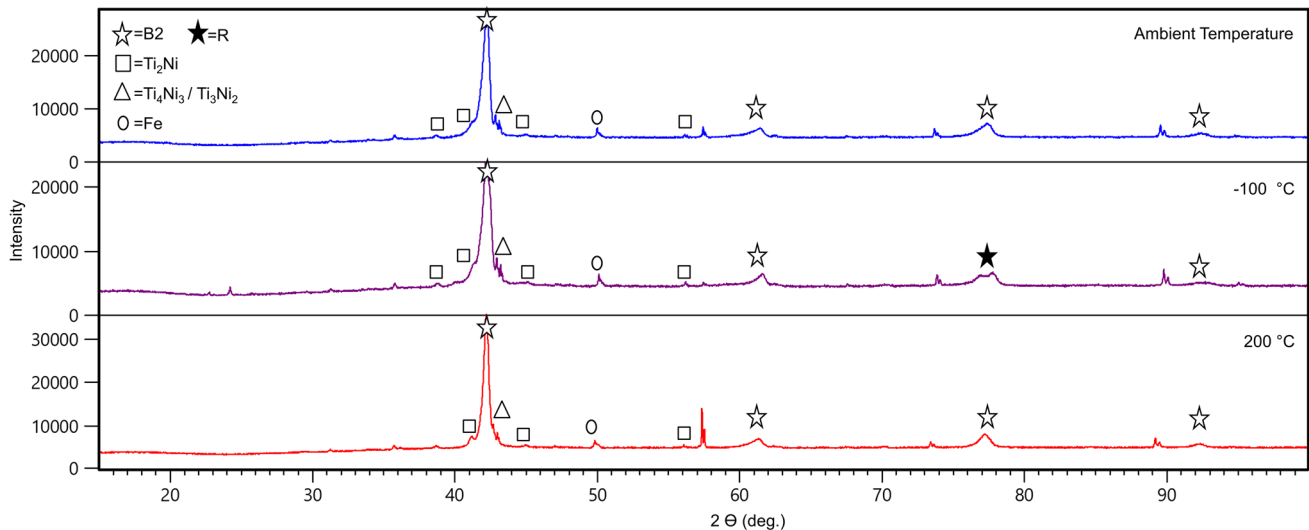


Fig. 7 XRD analysis of S330d5 for different (ambient, -100 and 200 °C) temperature

beside the main B2 peak (110). Therefore, the crystallite size of the main B2 phase peak of the samples was also calculated using the Scherrer formulation (see supplement file). S240d10 has the longest ignition duration, and its crystallite size exceeds that of S330d10. Additionally, according to Fig. 5, S240d10 appears brighter than S240d5 during the combustion stage. The subject has been studied very little, but Jin et al. found similar results in TiCx compound during SHS [28]. Although it may seem contradictory that the crystallite size of S330d10 (27 nm) is smaller than S240d10 (68 nm), a closer look at macrostructures indicates more liquefaction and compacting in S240d10, leading to lower internal porosity. Therefore, it can be said that the duration the ignition wire remains open (29.5 s.) has a more significant impact on the crystallite size. Similar interpretations can also be made according to the Scherrer formulation [35]. It should be emphasized that these calculations were made to roughly understand the impact of the ignition wire on the crystallite size, and Rietveld refinement may be required, but the grain size should ideally be in the micrometer (μm) scale. In future studies, a more in-depth investigation will be conducted using EBSD and TEM.

Despite yielding clear outcomes (like forcing complete propagation reaction) regarding porosity when using a triggering wire assisted SHS. It should be noted that the temperature and duration control of the ignition wire are not fully regulated. Nevertheless, these results are manageable.

At 200 °C, XRD diffraction shows the appearance of very sharp peaks. They cannot be associated with any of the relevant phases of martensite; consequently, can be attributed to secondary phases such as Ti_2Ni . Possibly their appearance after heating to 200 °C can be associated with a recovered metastable phase that formed during cooling after the

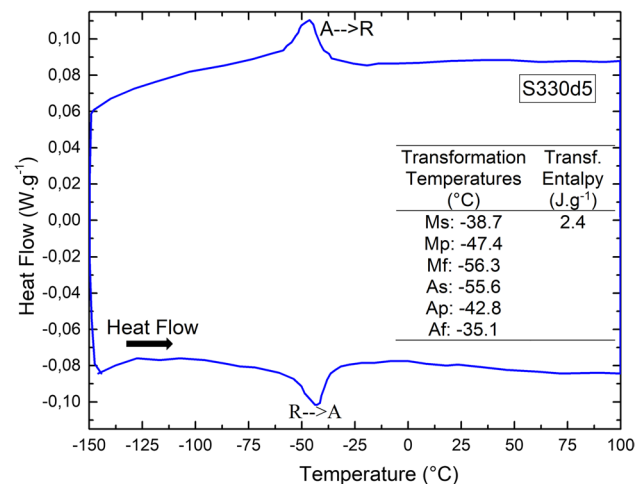


Fig. 8 DSC analysis of S330d5

reaction was completed. Unindexed peaks (as 57.52° etc.) are not relevant to any of the studied phases and possibly related to the crystallization of moisture or bakelite.

The martensite transformation temperature was not strictly connected to the preheating temperature as explained in the previous studies [13]. Therefore, two samples; S330d5 and S330d10 were preferred for the DSC analysis and sampled from the middle part of the specimen. Figure 8 shows the results of the thermal analysis, and the phase transformation values are given for S330d5. In S330d10, no transformation was observed. It was reported when the Fe ratio is increased, B2-R and R-B19' phases are more separated from each other, and B2-R transformation is prone to occur [8]. According to XRD analysis, the R phase is observed, while B19' is not. No transformation is observed for S330d10, and

martensitic transformation may be occurred below $-150\text{ }^{\circ}\text{C}$ [2]. There could be two reasons for it: (1) When Fe atomic ratio is increased in the B2 matrix, the Ms temperature decreases due to the antisite behavior of Fe in the B2 phase [10]. (2) The Ms temperature was affected by the ratio of nickel content. XRD and SEM analyses confirmed the formation of Ti_2Ni . Consequently, the Ms temperature experiences a significant reduction, accompanied by titanium depletion within the alloy. [2, 10, 36]. Nishida et al. showed that 4 at.% Fe decreased the Ms transformation temperature above 216 K ($-57\text{ }^{\circ}\text{C}$). Also, the R-B19' transformation was not observed after adding 3.2 at.% Fe to the B2 phase [8]. In the most recent study, Fukuda et al. showed that the transformation of the R-phase is not only athermal but also isothermal (time-dependent) in nature. Thus, the R-phase can be formed in $Ni_{44}Ti_{50}Fe_6$ when it is held at 150 K for a long time [37]. The transformation enthalpy of the R phase is low and found as 2.4 J.g^{-1} . It is compatible with results as demonstrated by previous studies (between 1.4 and 3.75 J.g^{-1}) [9, 38].

Figure 9 shows SEM images (with embedded EDS results) of the S330d5. Some porosities (circular black regions) can be observed in the microstructure due to the nature of the SHS process. Ti_2Ni phase is found to be dark grey and forms grain boundaries. Figure 9 provides confirmation that various segments (upper, middle, and bottom) of the specimen exhibit distinct phases and grain structures.

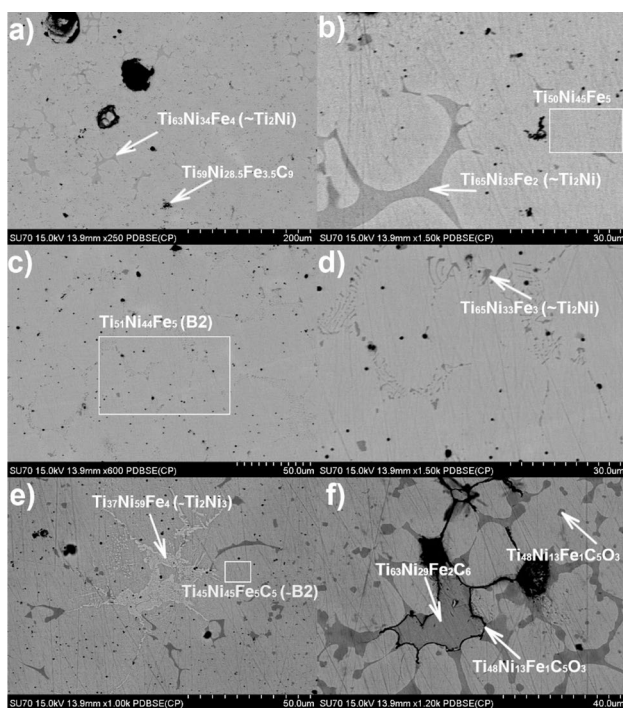


Fig. 9 BSE-SEM (wt. embedded EDS results) images for S330d5. **a–b** Bottom, **c–d** middle, **e–f** top section of the sample

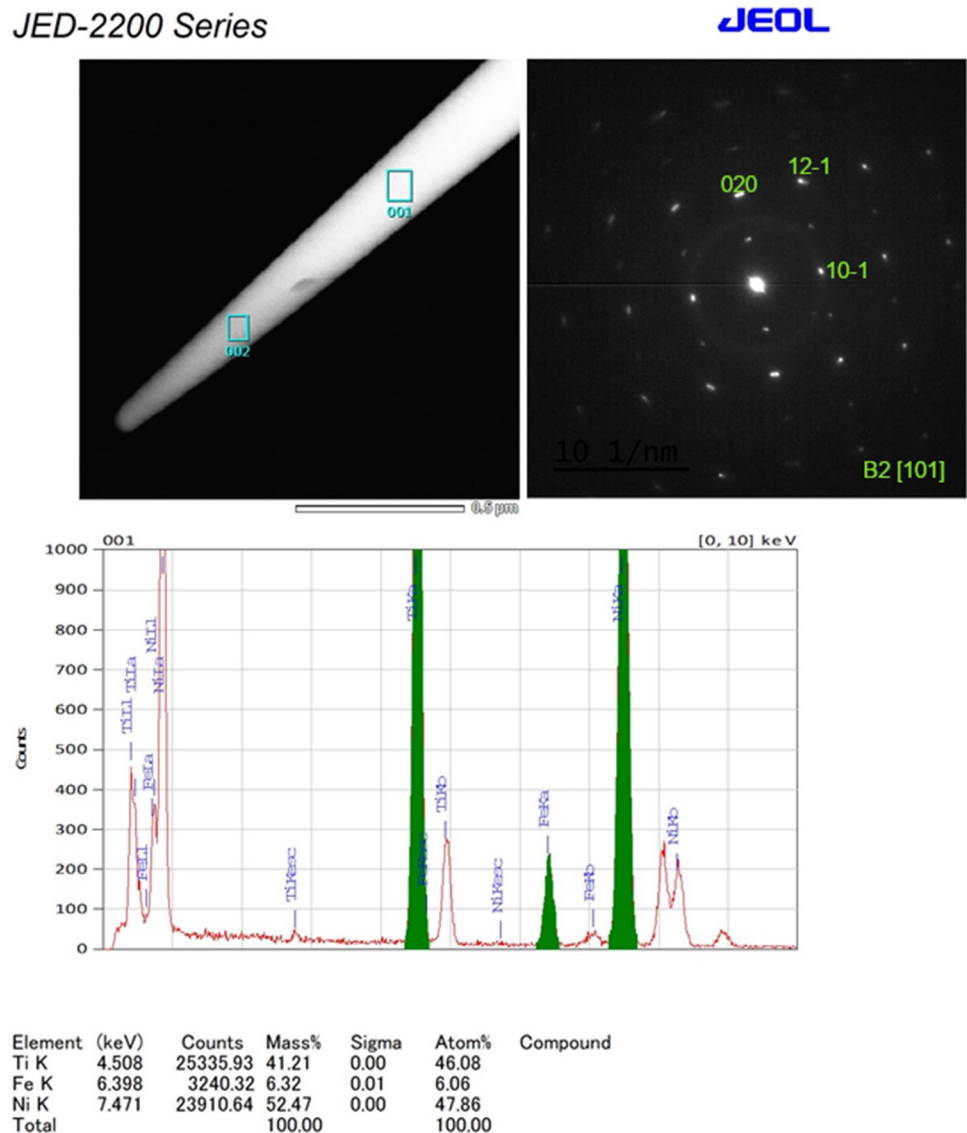
For instance, an inter-dendritic structure can be discerned within the overall microstructure. The dark gray points are $Ti_2(NiFe)$ which includes around 3 at.% Fe and the matrix formed as $Ni_{49.29}Ti_{45.64}Fe_{5.07}$. The Ti_2Ni and Ni_3Ti_2 phases are more prominent in the lower and upper parts, which are more affected by temperature. This situation can be explained by the fact that, during the initial solidification where the transition liquid is observed, nickel's diffusion rate is higher than that of titanium, resulting in the formation of Ti_2Ni structure alongside $NiTi$. C atoms are detected in the sample by SEM-EDS analysis, probably due to the carbon-coated ignition wire. C atoms are mostly found that are exposed to a higher temperature in the bottom and upper parts of the sample. The heat of the ignition wire affects the upper part while the preheating wire affects the sample more from the bottom than the top, and the propagating of the heating wave affects the bottom part due to the bounce back. As is well known, C atoms are smaller in diameter than Ti or Ni atoms, and their diffusion rate is very fast when compared to Ti and Ni . As a result, C is mostly diffused into various phases at the upper and bottom parts of the sample. In Fig. 9a, the black phase possible composition is the mixture of a minor amount of Ti_9C_9 and $Ti_{50}(Ni_{28.5}Fe_{3.5})\sim Ti_2Ni$.

Figure 10 shows the EDS analysis of the needle sample cut in from S330d5 by FIB. The atomic ratio of the sample was found as $Ni_{47.86}Ti_{46.08}Fe_{6.06}$. With the XRD results, the crystal structure was associated with a single crystal B2 that forms the matrix. In the diffraction indexing, the B2 phase is confirmed, and the plane and zone axes were shown in Fig. 10. Additionally, some diffusive peaks were detected near the B2 peaks, and these can be attributed to Ti_2Ni due to their similar crystal structures. It proves that B2 is the stable phase at room temperature, and it transforms to the R phase when the temperature is decreased to $-38.7\text{ }^{\circ}\text{C}$ according to the DSC analysis.

SEM images of sample S330d10, containing 10 at.% Fe, are depicted in Fig. 11. The images were taken from diverse regions to comprehensively analyze the structure. In certain areas, a significant inter-dendritic phase is noticeable, as illustrated in Fig. 11c. Meanwhile, circular rod-like formations of the Ti_2Ni phase are prevalent throughout the examined regions (Fig. 11d).

The phase distribution closely resembles that of S330d5, but the grain boundaries are more pronounced in S330d5 than in S330d10 according to the SEM images (Figs. 9 and 11) due to the reached higher combusting temperature. In essence, achieving a higher combustion temperature and the subsequent slow cooling within the closed chamber promotes grain growth and creates more Ti_2Ni phases in the grain boundaries. However, this assertion requires confirmation through further research by other investigators in the future.

Fig. 10 TEM-EDS spectral measurements from different phase-containing regions of the needle-shaped three-dimensional TEM sample prepared from sample S330d5



The remaining structure is confirmed to be the B2 phase through SEM-EDS analysis. As depicted in Fig. 12, TEM analysis is conducted for the needle-shaped specimen. The main phase is identified as polycrystalline B2 (Fig. 12d), with the presence of Ti_2Ni precipitates evident in Fig. 12e. Figure 12e–g depicts the elemental distribution of Ti–Ni–Fe. Fe demonstrates a uniform distribution across all samples (Fig. 12f), while the Ti-rich phase is localized at the corner of the sample (Fig. 12e). In the microstructure, the nano-crystalline grains are also observed in Fig. 12b. This observation indicates that the inherent nature of SHS does not yield a microstructure characterized by uniformly distributed equiaxed large grains, which can be attributed to the non-equilibrium conditions inherent in SHS reactions. TEM analysis reveals nanocrystalline precipitations in Fig. 12a–c. This is especially the case for NiTiFe products that undergo severe plastic deformation after rolling.

In other words, nanocrystalline and amorphous phase can be encountered in TEM analysis besides the grain size around ~ 10 microns in EBSD analysis after the sample is annealed (800°C) for 1 to 4 min. [39]. This situation can be adapted with the macro kinetics of SHS as follows: Merzhanov et al. observed first amorphization and then grain growth with heat in the liquid–solid transformation that occurs during the propagation. Considering that the propagation reactions are completed under 1 s., the outer part cools faster, while the inner part cools slowly by conserving heat [29]. As a result, the nanocrystalline (dark) and the amorphous section can be occurred due to not having enough time for recrystallization and grain growth. The nanocrystalline regions were observed in material containing 10 at.% Fe. It may also have a role in preventing the formation of the Ti_2Ni phase and grain growth by

Fig. 11 SEM-BSE images (wt. EDS embedded) of S330d10

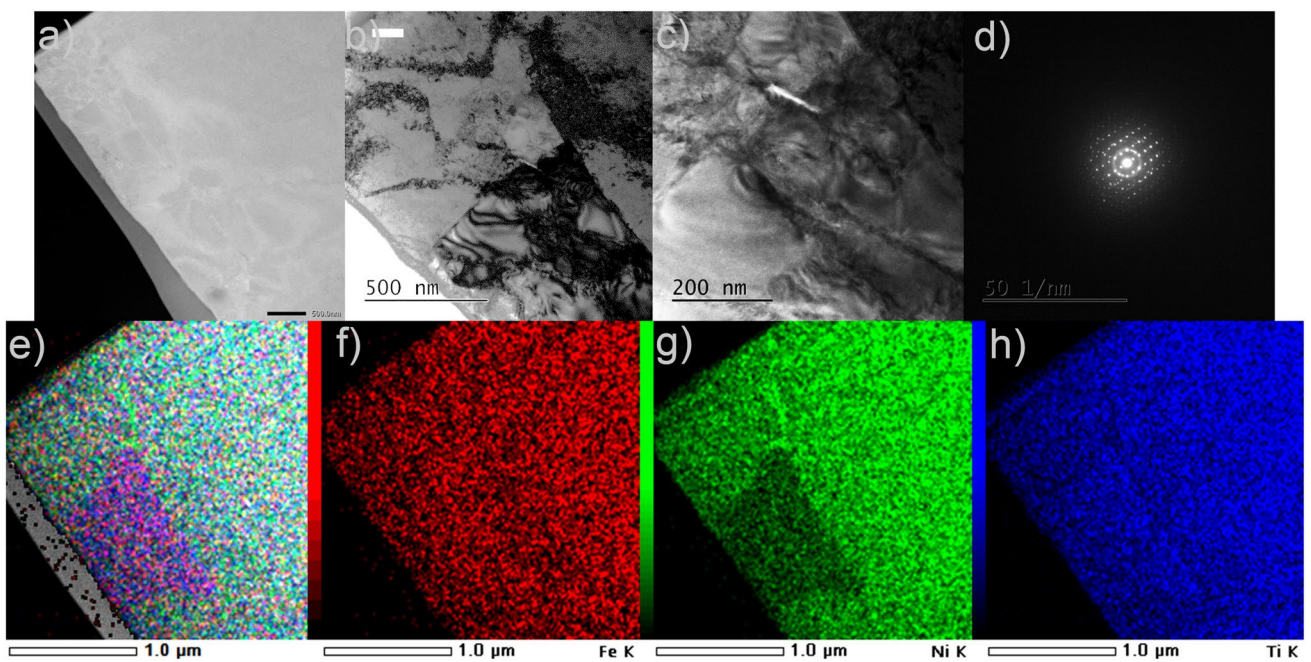
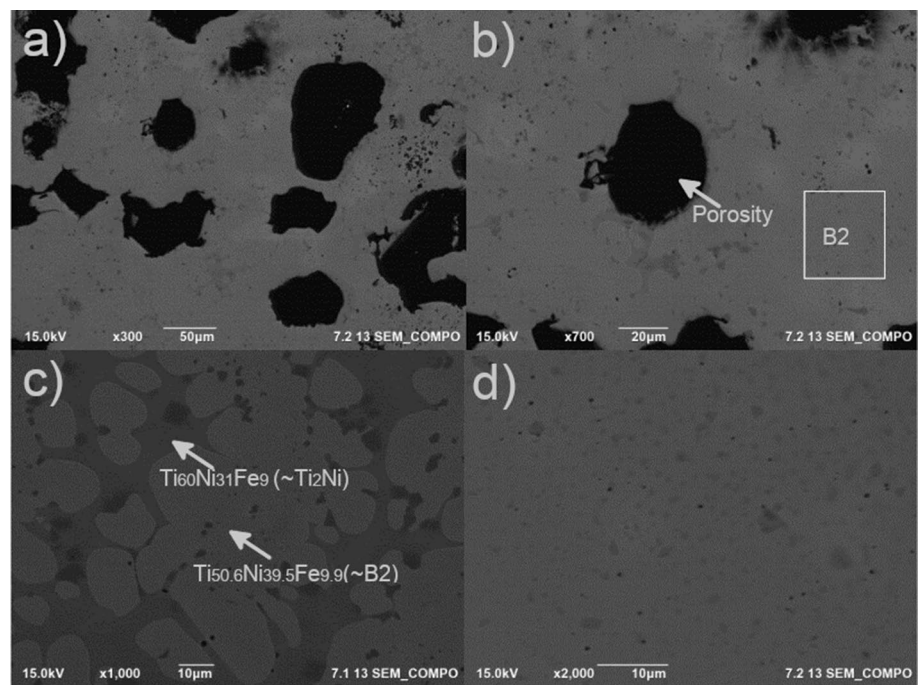


Fig. 12 TEM analysis of S330d10 **a** bright field, **b–c** dark field **d** diffraction spot **e–h** chemical analysis scanning of the sample

solid solution strengthening and should be investigated in future studies.

4 Conclusions

1. $\text{Ni}_{45}\text{Ti}_{50}\text{Fe}_5$ and $\text{Ni}_{40}\text{Ti}_{50}\text{Fe}_{10}$ were successfully synthesized from powder to bulk form at three different temperatures, namely 235–240 °C, 320–330 °C, and 410–420 °C. According to the calculated H/Cp val-

ues, the propagation probabilities of $\text{Ni}_{45}\text{Ti}_{50}\text{Fe}_5$ and $\text{Ni}_{40}\text{Ti}_{50}\text{Fe}_{10}$ are close to each other. However, the adiabatic temperatures attained, and the liquid/solid ratio play a role in influencing the resulting porosity. These values are challenging themselves with increasing Fe ratio in B2 phase as demonstrated using Factsage Software. The occurrence of unexpected small to medium-sized pores on the outer surface (as observed in S420d5 and S330d10) could be attributed to the low pressing pressure and heating rate during the process. It is also connected with inconsistency of temperature of ignition wire. It should be added that while forcing the completion of the reaction can be considered an advantage, the inability to control the W filament temperature may be seen as a drawback of the ignition wire assisted SHS. In addition to the combustion temperature and the duration of triggering the wire, the top and bottom sections, which are most sensitive to temperature changes, also influence the grain structure of the sample for upper, bottom, and middle section.

- The SEM analysis revealed a predominantly homogeneous structure. In both S330d5 and S330d10, the TiNi and Ti_2Ni phases exhibited a nearly equal distribution of Fe elements without compromising the NiTi ratio. The primary phase observed in the samples is the B2 phase. The B19' phase is not detected, and only the B2-R transformation is observed in the sample with 5 at.% Fe. The higher Fe ratio hinders the transformation from R to B19' within the studied temperature range. Interestingly, the presence of the Ni_4Ti_3 (or Ni_3Ti_2) phase has been identified, which further substantiates this transformation phenomenon.
- TEM analysis revealed a homogeneous distribution of Fe elements in the S330d10 sample, accompanied by the presence of B2 phases in both S330d5 and S330d10. While SEM analysis highlighted the presence of large grains, TEM analysis also identified nanocrystalline grains in the S330d10 sample.

5 Data availability statement

The datasets generated during and/or analyzed during the current study are available from the corresponding author on reasonable request.

Supplementary Information The online version contains supplementary material available at <https://doi.org/10.1007/s00339-024-07306-z>.

Acknowledgements The authors are pleased to acknowledge the financial support from The Scientific and Technological Research of Turkey (TUBITAK, Project No: 213M556). We thank to Dr. Feray Bakan Misirlioglu (SUNUM, Turkey), Dr. Meltem Bakan (SUNUM, Turkey) and Dr. Paola Bassani (CNR ICMATE, Italy) for helping in SEM cross-sections images and DSC investigations.

Author contributions All authors contributed to the study conception and design. Material preparation, data collection by BK and analysis were performed by BK and BD. The first draft of the manuscript was written by BK. All authors read and approved the final manuscript. All the authors have accepted responsibility for the entire content of this submitted manuscript and approved submission.

Funding Open access funding provided by the Scientific and Technological Research Council of Türkiye (TÜBİTAK).

Declarations

Conflicts of interest The authors declare that they have no conflict of interest. No potential conflict of interest was reported by the authors.

Open Access This article is licensed under a Creative Commons Attribution 4.0 International License, which permits use, sharing, adaptation, distribution and reproduction in any medium or format, as long as you give appropriate credit to the original author(s) and the source, provide a link to the Creative Commons licence, and indicate if changes were made. The images or other third party material in this article are included in the article's Creative Commons licence, unless indicated otherwise in a credit line to the material. If material is not included in the article's Creative Commons licence and your intended use is not permitted by statutory regulation or exceeds the permitted use, you will need to obtain permission directly from the copyright holder. To view a copy of this licence, visit <http://creativecommons.org/licenses/by/4.0/>.

References

- J.M. Jani, M. Leary, A. Subic, M.A. Gibson, A review of shape memory alloy research, applications and opportunities. *Mater. Design* **56**, 1078–1113 (2014)
- K. Otsuka, X. Ren, Physical metallurgy of Ti–Ni-based shape memory alloys. *Prog. Mater. Sci.* **50**(5), 511–678 (2005)
- P. Novák, P. Salvetr, A. Školáková, M. Karlík, J. Kopeček, Effect of alloying elements on the reactive sintering behaviour of NiTi alloy. *Mater. Sci. Forum* **891**, 447–451 (2017)
- E. Kassab, L. Neelakantan, M. Frotscher, S. Swaminathan, B. Maaß, M. Rohwerder, J. Gomes, G. Eggeler, Effect of ternary element addition on the corrosion behaviour of NiTi shape memory alloys. *Mater. Corros.* **65**(1), 18–22 (2014)
- G. Rondelli, Corrosion resistance tests on NiTi shape memory alloy. *Biomaterials* **17**(20), 2003–2008 (1996)
- G. Karthik, B. Kashyap, T.R. Prabhu, Processing, properties and applications of Ni-Ti-Fe shape memory alloys. *Mater. Today Proc.* **4**(2), 3581–3589 (2017)
- V. B. Krishnan, C. Bewerse, W. U. Notardonato, R. Vaidyanathan, U. Balachandran, K. Amm, D. Evans, E. Gregory, P. Lee, M. Osofsky, S. Pamidi, C. Park, J. Wu, M. Sumption, A Thermal Conduction Switch Based on Low Hysteresis Nitife Shape Memory Alloy Helical Springs. In *AIP Conference Proceedings*, p. 3–9 (2008)
- M. Nishida, T. Honma, Phase transformations in Ti50Ni50-xFex alloys. *Le J. de Physique Colloques* **43**(4), C4-225–C4-230 (1982)
- M.-S. Choi, J. Ogawa, T. Fukuda, T. Kakeshita, Stability of the B2-type structure and R-phase transformation behavior of Fe or Co doped Ti–Ni alloys. *Mater. Sci. Eng. A* **438**, 527–530 (2006)
- Y.-Q. Zhang, S.-Y. Jiang, X.-M. Zhu, Y.-N. Zhao, Y.-L. Liang, D. Sun, Influence of Fe addition on phase transformation behavior of NiTi shape memory alloy. *Trans. Nonferrous Metals Soc. China* **27**(7), 1580–1587 (2017)

11. J. Parida, S.C. Mishra, A. Behera, Synthesis and characterization of Ti50Ni (50– X) FeX alloy produced by mechanical alloying and pressure-less sintering. *Metals Mater. Int.* (2022). <https://doi.org/10.1007/s12540-022-01277-72022>
12. H.C. Yi, J.J. Moore, The combustion synthesis of Ni-Ti shape memory alloys. *JOM* **42**, 31–35 (1990)
13. H. Jiang, L. Rong, Ways to lower transformation temperatures of porous NiTi shape memory alloy fabricated by self-propagating high-temperature synthesis. *J. Mater. Sci. Technol.* **438**, 883–886 (2006)
14. J.J. Moore, H. Feng, Combustion synthesis of advanced materials: Part I reaction parameters. *Prog. Mater. Sci.* **39**(4), 243–273 (1995)
15. C.L. Yeh, W.Y. Sung, Synthesis of NiTi intermetallics by self-propagating combustion. *J. Alloys Compounds* **376**(1–2), 79–88 (2004)
16. B.Y. Tay, C.W. Goh, Y.W. Gu, C.S. Lim, M.S. Yong, M.K. Ho, M.H. Myint, Porous NiTi fabricated by self-propagating high-temperature synthesis of elemental powders. *J. Mater. Process. Technol.* **202**(1–3), 359–364 (2008)
17. A. Biswas, Porous NiTi by thermal explosion mode of SHS: processing, mechanism and generation of single phase microstructure. *Acta Materialia* **53**(5), 1415–1425 (2005)
18. S. Wisutmethangoon, N. Denmud, L. Sikong, Characteristics and compressive properties of porous NiTi alloy synthesized by SHS technique. *Mater. Sci. Eng. A* **515**(1–2), 93–97 (2009)
19. Y.-H. Li, L.-J. Rong, Y.-Y. Li, Pore characteristics of porous NiTi alloy fabricated by combustion synthesis. *J. Alloys Compounds* **325**(1), 259–262 (2001)
20. M.H. Elahinia, M. Hashemi, M. Tabesh, S.B. Bhaduri, Manufacturing and processing of NiTi implants: a review. *Progress Mater. Sci.* **57**(5), 911–946 (2012)
21. C.L. Chu, C.Y. Chung, P.H. Lin, S.D. Wang, Fabrication of porous NiTi shape memory alloy for hard tissue implants by combustion synthesis. *Mater. Sci. Eng. A* **366**(1), 114–119 (2004)
22. R.A. Ayers, S.J. Simske, T. Bateman, A. Petkus, R. Sachdeva, V. Gyunter, Effect of nitinol implant porosity on cranial bone ingrowth and apposition after 6 weeks. *J. Biomed. Mater. Res.* **45**(1), 42–47 (1999)
23. Z.A. Munir, U. Anselmi-Tamburini, Self-propagating exothermic reactions: the synthesis of high-temperature materials by combustion. *Mater. Sci. Rep.* **3**(7–8), 277–365 (1989)
24. W. Gaşior, A. Dębski, Enthalpy of formation of intermetallic phases from Fe-Ni-Ti system. *Compar. Stud. Arch. Metall. Mater.* **57**, 1095–1104 (2012)
25. E. Povoden-Karadeniz, D.C. Cirstea, P. Lang, T. Wojcik, E. Kozechnik, Thermodynamics of Ti–Ni shape memory alloys. *Calphad* **41**, 128–139 (2013)
26. P. Bellen, K.H. Kumar, P. Wollants, Thermodynamic assessment of the Ni-Ti phase diagram. *Int. J. Mater. Res.* **87**(12), 972–978 (1996)
27. B. Li, L.J. Rong, Y.Y. Li, V. Gjunter, Synthesis of porous Ni–Ti shape-memory alloys by self-propagating high-temperature synthesis: reaction mechanism and anisotropy in pore structure. *Acta Materialia* **48**(15), 3895–3904 (2000)
28. S. Jin, P. Shen, B. Zou, Q. Jiang, Morphology evolution of TiCx grains during SHS in an Al–Ti–C system. *Crystal Growth Design* **9**(2), 646–649 (2009)
29. A.G. Merzhanov, A.S. Rogachev, Structural macrokinetics of SHS processes. *Pure Appl. Chem.* **64**(7), 941–953 (1992)
30. G. Tosun, L. Ozler, M. Kaya, N. Orhan, A study on microstructure and porosity of NiTi alloy implants produced by SHS. *J. Alloys Compounds* **487**(1–2), 605–611 (2009)
31. R.R. Adharapurapu, F. Jiang, K.S. Vecchio, Aging effects on hardness and dynamic compressive behavior of Ti–55Ni (at.%) alloy. *Mater. Sci. Eng. A* **527**(7–8), 665–1676 (2010)
32. M. Kaya, N. Orhan, B. Kurt, T.I. Khan, The effect of solution treatment under loading on the microstructure and phase transformation behavior of porous NiTi shape memory alloy fabricated by SHS. *J. Alloys Compounds* **475**(1–2), 378–382 (2009)
33. X. Wang, B. Verlinden, J. Van Humbeeck, R-phase transformation in NiTi alloys. *J. Mater. Sci. Technol.* **30**(13), 1517–1529 (2014)
34. P. Li, Microstructure and mechanical properties of as-cast Ti–Ni–Fe alloys. *Mater. Res. Express* (2019). <https://doi.org/10.1088/2053-1591/ab58d8>
35. C. Suryanarayana, M. G. Norton, C. Suryanarayana, M. G. Norton, Practical aspects of X-ray diffraction. *X-ray diffraction: A practical approach.* (1998), pp.63–94
36. G.S. Firstov, J. Van Humbeeck, Y.N. Koval, High-temperature shape memory alloys. *Mater. Sci. Eng. A* **378**(1–2), 2–10 (2004)
37. T. Fukuda, M. Todai, T. Kakeshita, Isothermal martensitic transformation of the R-phase in a Ti–44Ni–6Fe at% alloy. *Scripta Materialia* **69**(3), 239–241 (2013)
38. E. Goo, R. Sinclair, The B2 to R transformation in Ti50Ni47Fe3 and Ti49 5Ni50.5 alloys. *Acta Metallurgica* **33**(9), 1717–1723 (1985)
39. Y. Zhang, S. Jiang, S. Wang, D. Sun, L. Hu, Influence of partial static recrystallization on microstructures and mechanical properties of NiTiFe shape memory alloy subjected to severe plastic deformation. *Mater. Res. Bull.* **88**, 226–233 (2017)

Publisher's Note Springer Nature remains neutral with regard to jurisdictional claims in published maps and institutional affiliations.